

Analysis of total-internal-reflection phase-conjugate mirror

A. A. Zozulya, G. Montemezzani, and D. Z. Anderson

Joint Institute for Laboratory Astrophysics, University of Colorado, C.B. 440, Boulder, Colorado 80309-0440

(Received 2 February 1995)

The geometry of a total-internal-reflection (TIR) phase-conjugate mirror is investigated in the framework of a two-dimensional model, based on the solution of nonlinear material equations and the parabolic equations for electromagnetic radiation. The model self-consistently describes the evolution of incoherent scattering into the spatial structure of light corresponding to the operation of the TIR mirror. We analyze the dynamics of nonlinear reflectivity and conjugation fidelity and their dependence on parameters of the problem, the spatial structure of fields and the nonlinear refractive index, and the typical distortions in the phase-conjugate output of the TIR mirror. Theoretical predictions are confirmed experimentally.

PACS number(s): 42.65.Hw, 42.50.Na

I. INTRODUCTION

The total-internal-reflection (TIR) phase-conjugate mirror [1] is probably the most widely used and definitely the most enigmatic among self-pumped geometries for phase conjugation and mutual conjugation in photorefractive nonlinear media. For an experimental photograph of this geometry in operation the reader is referred to Ref. [1]. In this geometry the incident beam entering the crystal undergoes asymmetric stimulated photorefractive scattering (fanning) [2], generating a broad fan of light emanating from the beam on one of its sides. The beam is aligned in such a way that this fan of light is directed toward one of the corners of the crystal. This corner acts as a retroreflector, returning the light back toward the primary beam. In photorefractive as in any other nonlinear optical media, light changes the refractive index of the medium, which in turn changes the light distribution. As a result of the development of this process, the fan collapses into one or several loops. The geometry generates a scattered beam, which leaves the crystal back along the direction of the incident beam and is its phase-conjugate replica.

The TIR mirror turned out to be among the most challenging phase-conjugation geometries from a theoretical point of view, and thus its theoretical description is practically nonexistent. A one-dimensional plane-wave model of the TIR mirror was proposed in Ref. [3]. It visualizes the TIR mirror as consisting of two four-wave mixing regions coupled via boundary conditions. Later analyses have shown that in the framework of this model the TIR mirror belongs to the family of four-wave mixing geometries with hard excitation thresholds. The dynamics of these geometries is determined by a finite level of noise (seeds) necessary for their self-start (see, e.g., Ref. [4] and references therein). The above theoretical analyses resulted in insights into some features of the TIR mirror, but due to the complexity of the geometry, the analyses relied on *ad hoc* assumptions about the structure of the electromagnetic fields inside the medium. There has been no theory that would be able to self-consistently describe the evolution of incoherent scattering into the spatial structure of light corresponding to the operation of the TIR mirror and predict, for example, the values of nonlinear reflectivity and conjugation fidelity.

Recent papers [5–8] proposed a direct numerical ap-

proach for the investigation of light propagation in photorefractive media. This approach turned out to be a powerful tool for analyzing the formation of complex structures of light corresponding to fanning and the self-pumped geometries for phase conjugation and mutual phase conjugation [6].

This paper is devoted to the theoretical analysis of the TIR mirror in the framework of a two-dimensional model based on the solution of nonlinear material equations and the parabolic equations for electromagnetic radiation. We do not make any *a priori* assumptions about the spatial structure of light to be generated inside the photorefractive medium, and we specify only the input amplitude distribution of a light beam incident onto a crystal. The evolution of the beam inside the crystal is governed by diffraction and material nonlinearity. Results of our analysis are presented in subsequent sections and may be summarized as follows.

(1) The model self-consistently describes the development of incoherent scattering into the spatial structure of light corresponding to the formation of the TIR mirror geometry. The calculated spatial distributions of the intensity of light and the nonlinear refractive index inside the medium indicate that the TIR mirror is a distributed phase conjugator with the conjugation taking place not only in the main body of the beam but also inside the fanning loops.

(2) We calculate and analyze the dynamics of nonlinear reflectivity and conjugation fidelity. It is shown that the TIR mirror requires a finite level of seeding (noise) for its efficient operation. The dependence of the reflectivity and the conjugation fidelity on the level of these seeds is discussed.

(3) The near-field transverse distribution of the output radiation and its Fourier spectrum (far-field distribution) are analyzed in detail. Phase conjugation in the geometry of the TIR mirror (as in any other real system) is not ideal and in general is accompanied by distortions in both the space and Fourier domains. The dependence of these distortions on the parameters of the problem is revealed.

(4) The theoretical predictions pertaining to the space and Fourier domain distortions are confirmed in experiment.

II. BASIC EQUATIONS

The photorefractive material response of the medium is governed by the set of equations [9]

$$\frac{\partial}{\partial t} N_D^+ = (\beta + s I_{em})(N_D - N_D^+) - \xi n_e N_D^+, \quad (1a)$$

$$\nabla \cdot \epsilon_0 \hat{\epsilon} \vec{E} = e(N_D^+ - N_A - n_e), \quad (1b)$$

$$\nabla \cdot \left(\epsilon_0 \hat{\epsilon} \frac{\partial}{\partial t} \vec{E} + e \mu n_e \vec{E} + \kappa_B T \mu \nabla n_e \right) = 0. \quad (1c)$$

Here N_D, N_D^+, N_A , and n_e are the densities of donors, ionized donors, acceptors, and electrons, respectively; \vec{E} is the amplitude of the static electric field; e is the electron charge; ϵ_0 is the dielectric permeability of vacuum; $\hat{\epsilon}$ is the static dielectric tensor; ξ is the recombination constant; μ is the electron mobility; κ_B is Boltzmann's constant; T is the temperature; β and s are the thermal and photoexcitation coefficients, respectively; and I_{em} is the intensity of electromagnetic radiation. We assume that all functions in Eqs. (1) predominantly change along one direction, which we denote as the y axis, and so all differential operators are replaced by a partial derivative along this direction. We introduce the characteristic Debye wave number $k_D = (e^2 N_A / \kappa_B T \epsilon_0 \epsilon_{eff})^{1/2}$ (where $\epsilon_{eff} = \vec{e}_y \hat{\epsilon} \vec{e}_y$, and \vec{e}_y is the unity vector along y), the normalized density of ionized donors $N = N_D^+ / N_A$, and the normalized amplitude of the electric field $\nu = E / \tilde{E}$, where $\tilde{E} = \kappa_B T k_D / e \equiv e N_A / \epsilon_0 \epsilon_{eff} k_D$. Under the assumptions of $N_D \gg N_A \gg n_e$ and $\mu e / \epsilon_0 \epsilon_{eff} \xi \ll 1$, Eqs. (1) may be rewritten in the form

$$n_e = \frac{N_D}{\xi N N_A} (s I_{em} + \beta), \quad (2a)$$

$$\frac{1}{k_D} \frac{\partial}{\partial y} \nu = N - 1, \quad (2b)$$

$$\frac{\epsilon_0 \epsilon_{eff}}{e \mu} \frac{\partial}{\partial t} \nu + n_e \nu + \frac{1}{k_D} \frac{\partial}{\partial y} n_e = 0. \quad (2c)$$

Further, we introduce the normalized intensity of the electromagnetic radiation $I = (I_{em} + \beta/s) / I_0 \equiv \tilde{I}_{em} + I_d$, where I_0 is some characteristic intensity (e.g., at the center of the beam) and I_d is the normalized dark intensity due to thermal excitation of carriers and/or possible incoherent erasure intensity. With this definition, the set of equations (2) reduces to one equation for the normalized amplitude of the static electric field:

$$I^{-1} \left(1 + \frac{1}{k_D} \frac{\partial \nu}{\partial y} \right) \frac{\partial}{\partial \tau} \nu + \nu - \frac{1}{(k_D)^2} \frac{\partial^2 \nu}{\partial y^2} \left(1 + \frac{1}{k_D} \frac{\partial \nu}{\partial y} \right)^{-1} = - \frac{1}{k_D} \frac{\partial}{\partial y} \ln I, \quad (3)$$

where $\tau = t/t_0$, $t_0 = \epsilon_0 \epsilon_{eff} \xi N_A / e \mu s I_0 N_D$, is the characteristic relaxation time of the static electric field.

The equations governing propagation of the optical fields have the form

$$\left(\frac{\partial}{\partial x} - \frac{i}{2k} \frac{\partial^2}{\partial y^2} \right) A_f = 2i \gamma_0 \nu A_f, \quad (4a)$$

$$\left(-\frac{\partial}{\partial x} - \frac{i}{2k} \frac{\partial^2}{\partial y^2} \right) A_b = 2i \gamma_0 \nu A_b, \quad (4b)$$

where k is the wave number of electromagnetic radiation inside the medium, A_f and A_b are forward and backward propagating electromagnetic fields, respectively, and γ_0 is the nonlinearity constant. Equations (4) are written in the paraxial approximation, that is, the angles of propagation of all beams with respect to the x axis are assumed to be small compared to unity. The same paraxial approximation ensures that all functions in Eqs. (1) predominantly change along the y direction. The intensity of the electromagnetic radiation I in Eq. (3) is $I = |A_f|^2 + |A_b|^2 + I_d$. Note that Eqs. (3) and (4) do not contain terms corresponding to reflection-type gratings, which result in direct backscattering.

For their operation, all self-pumped phase-conjugation geometries require, besides nonlinearity, a sufficiently large amount of background low-intensity broadband electromagnetic radiation (noise). This noise provides seeds for generating the spatial structures of light corresponding to the formation of these geometries. Amplification of this noise, in particular, is responsible for the incoherent stimulated photorefractive scattering (fanning) (for experimental results on fanning see, e.g., Refs. [10–12]). The noise is usually supplied by the beam itself. It may be due to volume scattering of the beam inside the medium from the inhomogeneities of the refractive index or to surface scattering from imperfections on the crystal faces. The noise may also be present on the input beam if, for example, it passes through an aberrator before entering the medium or if its Fourier spectrum is broad enough. We implemented different kinds of surface and volume seeding and found them to give qualitatively the same results. The results presented below correspond to distributed volume seeding, which was implemented via a series of phase screens distributed throughout the medium. In passing through a screen the light amplitude is multiplied by a random phase $\exp[i\varphi(y)]$, where $\varphi(y)$ is a random Gaussian function characterized by the mean square $\langle \varphi^2 \rangle = \epsilon / N_s$ (where ϵ is a small parameter and N_s is the number of screens) and the correlation length l_N or, equivalently, by the characteristic divergence angle θ_N in Fourier space. Different screens are uncorrelated. In the presence of the noise but without nonlinearity ($\gamma_0 = 0$) the Fourier spectrum of a Gaussian beam having passed through the medium consists of a kernel and a low-intensity noise pedestal. The relative power of the incident beam going into this pedestal is about ϵ times that of the kernel. For numerical analysis of fanning in the framework of this model, see [13]; a different implementation of noise has been analyzed in [14].

The boundary conditions for the system of equations (3) and (4) correspond to specifying the input amplitude distribution of a light beam entering the crystal and to imposing reflective boundary conditions at the crystal faces. The reflection is described phenomenologically. The input face is assumed to be transparent and the side faces ideally reflecting. The radiation $A_f(x=l_x, y)$ incident at the back crystal face $x=l_x$ is decomposed into Fourier harmonics. Those in-

cident at angles larger than $\theta_{TIR} = 10^\circ$ undergo total internal reflection; the rest are reflected with a reflectivity coefficient equal to $(n-1)^2/(n+1)^2$, where n is the linear refractive index of the crystal. The reflected radiation is transformed back into a space domain and gives the value of $A_b(x=l_x, y)$. Some runs have also been carried out with the radiation propagating at angles $\theta > \theta_{TIR}$ being totally reflected and the rest totally transmitted. No qualitative differences have been found between these cases.

Equations (3) and (4) were solved using a finite difference Crank-Nicholson-type scheme. To keep computational demands at a reasonable level, the dimensions of the nonlinear medium have been made smaller than in a typical experiment. The results discussed below (unless explicitly mentioned otherwise) were obtained using the slightly converging or diverging input Gaussian beam

$$A_{in}(y) \equiv A_f(x=0, y) = \exp[-4y^2/d^2 +iky^2/2R + i\theta_{in}ky], \quad (5)$$

where d is the diameter, R is the radius of curvature, and θ_{in} is the signed angle of incidence. Both R and θ_{in} are values inside the crystal.

The coordinate system has been chosen in such a way that the beam enters at $x=0$ and propagates in the direction of the positive x axis; the direction of energy transfer (fanning) coincides with the direction of the positive y axis. The size of the computation region is $l_x = 1.5$ mm and $l_y = 0.52$ mm along the x and y coordinate axes, respectively; beam diameter $d = 0.14$ mm; beam incidence angle $\theta_{in} = 2^\circ$; nonlinearity $\gamma_0 l_x = 11$; refractive index $n = 2.3$; radiation wavelength $\lambda = 0.514$ μm ; $k_D/k_0 \equiv k_D \lambda / 2\pi = 0.4$; normalized dark intensity $I_d = 0.01$; and characteristic divergence of noise $\theta_N = 20^\circ$. The radius of curvature of the beam R is equal to either $-7 l_x$ for the converging beam or $+7 l_x$ for the diverging beam.

The integral output characteristics of the geometry were characterized by the nonlinear reflectivity R and the conjugation fidelity H , determined by the relations

$$R = \frac{\int dy |A_{conj}(y)|^2}{\int dy |A_{in}(y)|^2}, \quad (6a)$$

$$H = \frac{|\int dy A_{conj}(y) A_{in}(y)|^2}{(\int dy |A_{conj}(y)|^2)(\int dy |A_{in}(y)|^2)}. \quad (6b)$$

The total output electromagnetic field $A_b(x=0, y)$, in addition to the phase-conjugate beam, contains contributions from the part of the incident beam that propagates without interaction to the back face of the crystal, is partially reflected, and returns back to the input face. It also contains large-angle fanning reflected from the side and back faces of the crystal. Both these contributions are usually not accounted for in calculating and/or measuring the nonlinear reflectivity and the conjugation fidelity (6). To separate the backscattered conjugate beam from the reflected incident beam and large-angle fanning we used a window in Fourier space centered at the spatial frequency corresponding to the nominal direction of propagation of the backscattered beam, with the width of the window considerably exceeding the characteristic angular divergence of the incident beam but

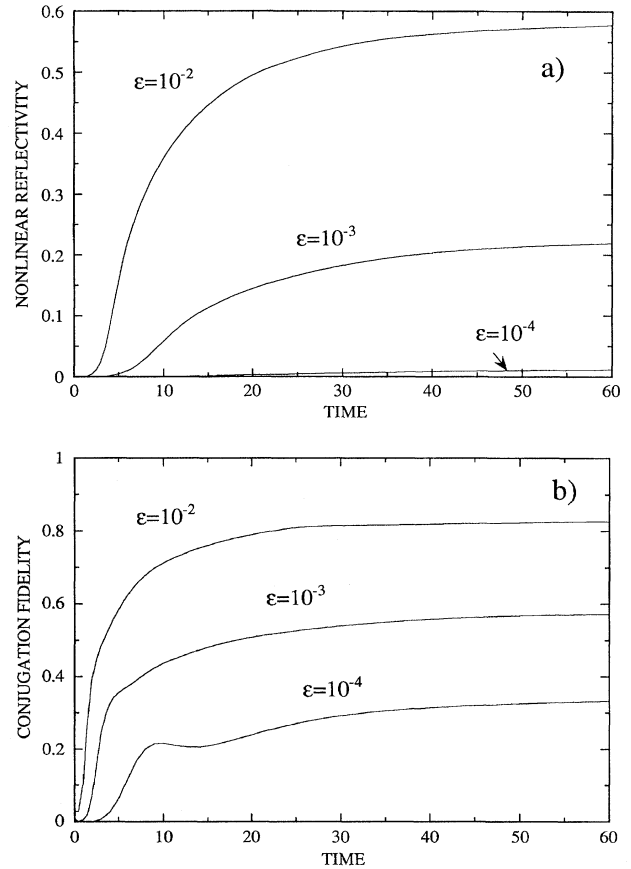


FIG. 1. Dynamics of (a) the nonlinear reflectivity and (b) conjugation fidelity for values of volume seeding $\epsilon = 10^{-2}$, 10^{-3} , and 10^{-4} .

less than the angular separation between this beam and its linear reflection. The part of the total output field $A_b(x=0, y)$ with the Fourier spectrum inside this window is considered to be a backscattered conjugate beam $A_{conj}(y)$ entering relations (6). Its coordinate distribution is obtained by the inverse transform of the spectrum inside the window. In the calculations that follow, the width of the Fourier window was taken to be 3° .

III. NUMERICAL RESULTS

Figures 1(a) and 1(b) show the time evolution of the nonlinear reflectivity R and the conjugation fidelity H , respectively, in the geometry of a TIR phase conjugator for the converging beam and for values of volume seeding $\epsilon = 10^{-2}$, 10^{-3} , and 10^{-4} . Calculations for the diverging beam gave very similar results. These figures demonstrate that the TIR mirror requires a finite level of seeds (noise) for its operation. Both reflectivity and conjugation fidelity are directly dependent on the level of seeding and decrease when this level is decreased. For $\epsilon = 10^{-4}$, the TIR mirror is close to the observable threshold of its operation, since the nonlinear reflectivity remains close to zero. The run with $\epsilon = 10^{-4}$ has been continued up to $t = 120$; the nonlinear reflectivity remained at about 1.3%. We have also carried out calculations with surface seeding and for an input beam hav-

ing a random (speckle) structure, for which the qualitative dependence of the reflectivity and the conjugation fidelity on the level of seeds remained the same.

We have found that phase conjugation in the geometry of the TIR mirror is accompanied by reproduction of small-scale structure and by large-scale distortions of the beam envelope both in space and in Fourier domains, or, in other words, intensity and phase distortions. The magnitude of these distortions is larger for small values of nonlinearity and/or level of seeds, and decreases when either of these parameters is increased. Higher values of nonlinear reflectivity and conjugation fidelity correspond to smaller distortions. The distortions are typical for practically all self-pumped four-wave mixing geometries. Their physical reason is the noncollinear nature of the interaction and the finite transverse size of the beams [7,15]. The distortions of the intensity profile of the conjugate beam seen in the space domain correspond to its lateral shift in the direction of the convective flow of energy for the scattered radiation (the direction of fanning). The phase distortions that manifest themselves in the Fourier domain correspond to a shift in the spectrum of the conjugate beam with respect to that of the incident one. In other words, the conjugate beam does not exactly counterpropagate with respect to the incident one. The output direction of propagation may lie on either side of that of the incident beam and is determined mostly by the focusing conditions.

Figure 2(a) shows the intensity distribution of the input (dashed) and output (solid) radiation at the entrance face of the crystal $x=0$ for $\epsilon=10^{-2}$ and for the converging beam. The dashed curve is the input Gaussian. The total output intensity $I_{b,out} \equiv |A_b(x=0,y)|^2$ consists of several distinct maxima of different physical origins. The small hump in output on the right-hand side of the dashed curve is the part of the incident beam that propagates through the crystal without interaction, is linearly reflected from the back surface, and returns to the input face. The intensity hump on the right close to the side face is the large-angle fanning reflected from the back and side surfaces (the beam fans toward the direction of the positive y axis). The part of the output radiation spatially overlapping with the input beam is the backscattered conjugate beam.

The Fourier spectrum of the output radiation around the nominal direction of propagation of the backscattered beam for the parameters of Fig. 2(a) is shown in Fig. 2(b) (solid curve). The calculations are carried out inside the medium; the corresponding propagation angles outside are $n=2.3$ times larger. The Fourier window is centered at the spatial frequency corresponding to the angle $\theta_{out} = -\theta_{in}$, where $\theta_{in}=2^\circ$ is the angle of incidence of the input beam. The dashed curve is the Fourier spectrum of this beam, inverted in Fourier space around zero spatial frequency to allow direct comparison to the spectrum of the backward propagating beam. The intensity profile of the backpropagating beam recovered by the inverse Fourier transform inside the 3° window of Fig. 2(b) is shown in Fig. 2(c).

The Fourier intensity spectrum of the output radiation inside the Fourier window for the diverging beam and all parameters of Fig. 2 is shown in Fig. 3(a). The intensity profile of the backpropagating beam recovered by the inverse Fourier transform inside the window of Fig. 3(a) is shown in Fig.

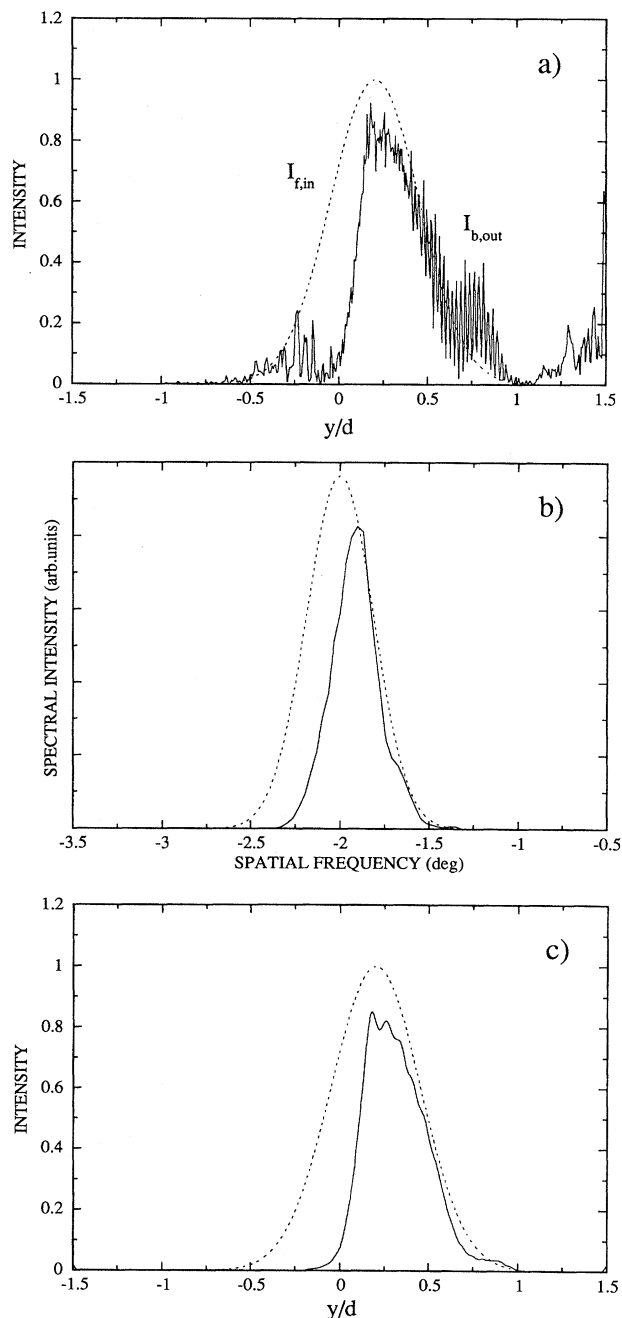


FIG. 2. Intensity distribution of (a) the total output radiation, (b) the Fourier intensity spectrum near the nominal direction of propagation of the conjugate beam, and (c) the intensity distribution of the conjugate beam. The beam is converging, and the value of seeds $\epsilon=10^{-2}$.

3(b). The intensity distribution of the total output radiation for the diverging beam is very similar to that of Fig. 2(a) and is not shown. The values of nonlinear reflectivity and conjugation fidelity for the diverging and converging beams differ by several percent.

Figures 2 and 3 demonstrate that for both the converging and the diverging beams the distortions in the space domain

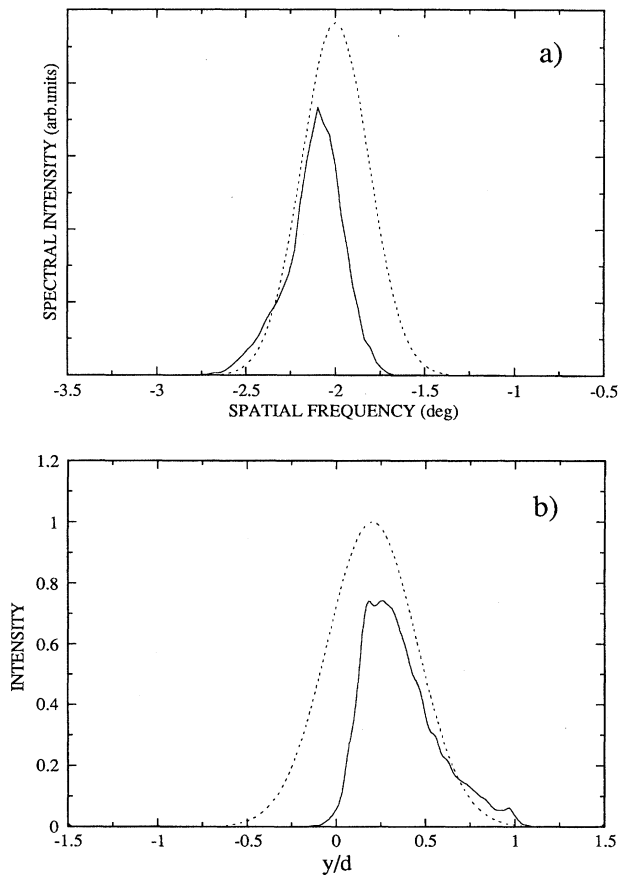


FIG. 3. (a) Fourier intensity spectrum near the nominal direction of propagation of the conjugate beam and (b) the intensity distribution of the conjugate beam. The beam is diverging; all other parameters are as in Fig. 2.

are of the same nature: the spatial profile of the conjugate beam is shifted in the direction of fanning. The distortions in the Fourier domain are quite different and determined by the focusing conditions. The converging incident beam produces the phase-conjugate beam propagating closer to the x axis than this incident beam ($|\theta_{out}| < |\theta_{in}|$). For the diverging beam the situation is the opposite ($|\theta_{out}| > |\theta_{in}|$). The distortions in the Fourier domain are lowest for an approximately collimated beam with its waist lying inside the crystal, but are also determined to a certain extent by the exact amplitude distribution of the incident beam.

Phase conjugation of a spatial structure imprinted on the input beam is demonstrated by Fig. 4, analogous to Figs. 2(c) and 3(b). The input beam in this case is the converging cosine-modulated Gaussian $A_{in}(y) = \cos(10y/d) \exp[-4y^2/d^2 - ik_y^2/2R + i\theta_{in}ky]$, $\epsilon = 5 \times 10^{-2}$; all other parameters are as in Figs. 2 and 3. This figure demonstrates that the fine-scale spatial information imprinted on the beam is reproduced, and that the distortions are indeed large-scale distortions of the envelope.

The spatial distributions of light intensity for the level of seeds $\epsilon = 10^{-2}$ at times $t = 5$ and $t = 60$ are presented in Figs. 5(a) and 5(b), respectively. The beam is convergent; for the diverging beam the picture looks very similar. The evolution

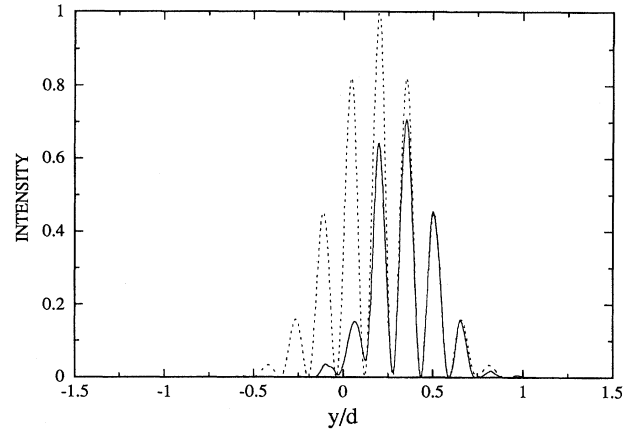


FIG. 4. Intensity distribution of the conjugate beam for the input cosine-modulated converging Gaussian beam and for $\epsilon = 5 \times 10^{-2}$.

of the spatial structure of light in the geometry of a TIR mirror is as follows. Initially the incident beam undergoes asymmetric incoherent scattering (fanning). The scattered radiation is directed toward the upper right corner of the crystal, serving as a retroreflector. The reflected light intersects the primary beam, forming a series of loops. The loops are formed primarily in the vicinity of the corner itself, but at later times the region occupied by the loops expands and moves toward the input face of the crystal [Fig. 5(a)]. The intensity of the loops grows with time. When the intensity of light channeled out into the loops becomes large enough, the loops start to compete for the energy of the pumping beam. The number of loops and the region occupied by them gets smaller, and each one of the remaining loops becomes thicker and brighter. In the final stage of evolution the light fanned out of the primary beam is channeled into a few very bright, relatively narrow loops. The average intensity inside the loops can exceed that in the input beam by several times. For example, the intensity inside the loops in Fig. 5(b) is about six times higher than the maximum input intensity of the Gaussian beam. The spatial structure of the radiation propagating in the loops is characterized by small characteristic scales and large gradients.

Figure 5(c) shows the steady-state spatial distribution of the nonlinear refractive index (its modulus) corresponding to the intensity distribution of Fig. 5(b). This distribution is considerably wider than that of the light and covers practically all of the region between the beam and the upper face of the crystal. The reason is that the amplitude of the refractive index change in photorefractive media is determined not by the intensity of light, but rather by its spatial derivative, as is seen from relation (3). Even a low-intensity light results in relatively large amplitudes of the refractive index if small spatial scales are involved. The moduli of the amplitude of the refractive index in the regions with high or low intensity differ on the average by no more than a factor of two. Figure 5(b) shows that the spatial distributions of intensity and the refractive index in the geometry of the TIR mirror are loosely correlated. The same distributions are more strongly correlated for the geometry of the double phase-conjugate mirror [7,16] or for fanning of a single light beam sufficiently far from reflecting surfaces.

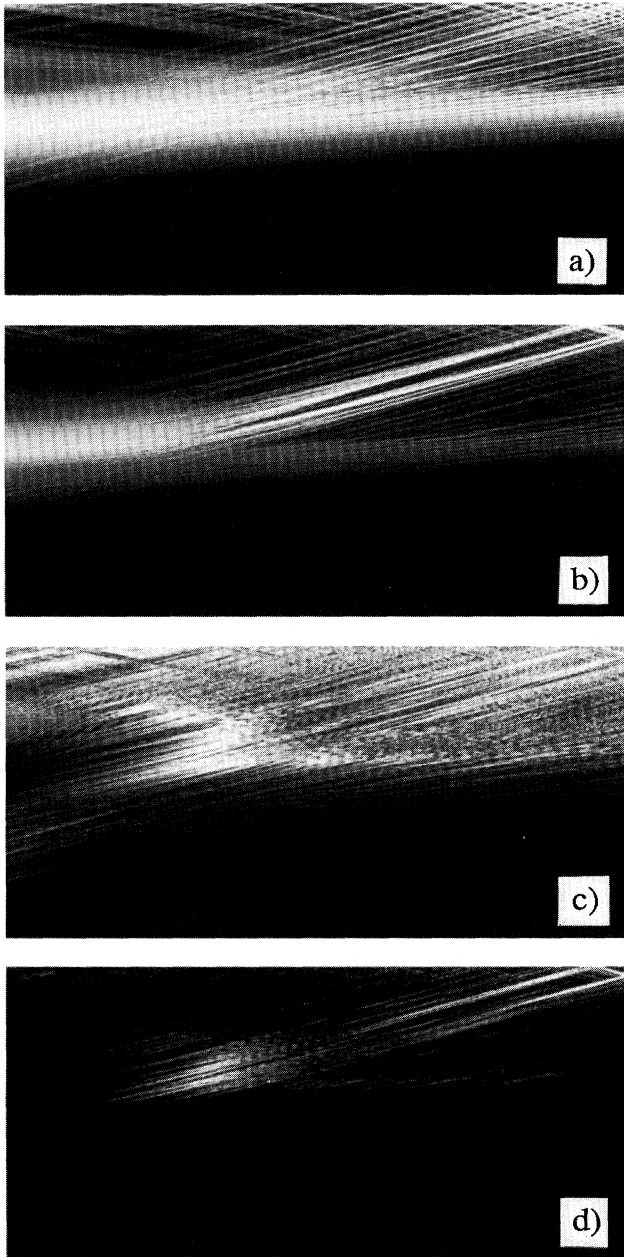


FIG. 5. Spatial distribution of the total light intensity $\tilde{I}_{em} = |A_f|^2 + |A_b|^2$ inside the crystal for (a) $t=5$ and (b) $t=60$; (c) spatial distribution of the modulus of the refractive index ν for $t=60$; and (d) the product $P = \tilde{I}_{em} \nu^2$ for $t=60$. The size of the computation region for all figures is $l_x = 1.5$ mm and $l_y = 0.52$ mm along the x and y coordinate axes, respectively.

Figure 5(d) shows the spatial distribution of the product of the intensity and the square of the refractive index $P = (|A_f|^2 + |A_b|^2) \nu^2$. This quantity may be visualized as the efficiency of nonlinear scattering and is useful in understanding what parts of the crystal contribute most in the formation of the TIR mirror. The function P is mostly localized in the region where the loops intersect the body of the incident beam and along the loops themselves. The characteristic values of P along the loops are about 1.5–2 times higher. Fig-

ure 5(d) indicates that the TIR mirror is a distributed phase conjugator. The phase conjugation takes place not only in the body of the main beam, but also inside the loops. This conclusion may be understood better by noticing that each of the loops is formed by two counterpropagating bent beams and may be visualized as a double phase-conjugate mirror.

IV. EXPERIMENTS

To check the predictions of our model we performed phase-conjugation experiments in the TIR geometry using photorefractive BaTiO₃ crystals. The presence of the near-field, large-scale intensity distortions of the phase-conjugate beam has been demonstrated in the following experiment. The spatial information of a resolution chart was put on the input beam entering the TIR mirror. The chart was imaged by a single $f = 150$ mm lens to a plane lying 220 mm beyond the lens. The phase-conjugating crystal was placed at different positions along the input beam path. The phase-conjugate image was deflected by a beam splitter onto a screen placed at the position corresponding to the image plane of the resolution chart. The image of the chart imprinted on the input beam is shown in Fig. 6(a).

When the crystal is placed in the image plane of the chart, the optical system images the input face of the crystal on the observation screen, allowing one to directly monitor the near-field intensity distribution of the phase-conjugate beam. Figures 6(b) and 6(c) correspond to this imaging case. They were obtained for two opposite directions of the c axis of the crystal, that is, with the beam fanning in opposite directions in the laboratory frame. Both figures demonstrate large-scale intensity distortions of the envelope of the output phase-conjugate beam. The distribution of the phase-conjugate light is shifted either to the left or to the right with respect to Fig. 6(a), depending on the direction of the c axis. In both cases the shift is in the direction of fanning inside the crystal, in agreement with the numerical predictions of Figs. 2(c) and 3(b). Figure 6 also shows a certain collapse of the reconstructed image in the vertical direction, perpendicular to the plane of incidence. This feature is not contained in our two-dimensional model because the beam is assumed to be infinitely wide in that direction. Note that the effective horizontal width of the input beam decreases with increasing vertical distance from the beam center. Therefore the above collapse may be phenomenologically explained by the decrease in reflectivity that we observed both experimentally and numerically by reducing the width of the input beam while keeping other parameters constant.

If the crystal is placed not in the image plane of the chart but in the Fourier plane, or somewhere in between, the restored phase-conjugate image observed on the screen looks better. This is illustrated by Fig. 6(d), which shows the reproduced image on the screen if the crystal is placed 40 mm before the image plane. The picture on the screen closely corresponds to the one transmitted through the chart [Fig. 6(a)], but the image resolution is slightly decreased. This behavior is not surprising considering the fact that the near-field intensity distortions are scrambled by the diffraction and smeared throughout the cross section of the beam. The good-looking image in these conditions does not, however, mean that the phase-conjugation fidelity is considerably

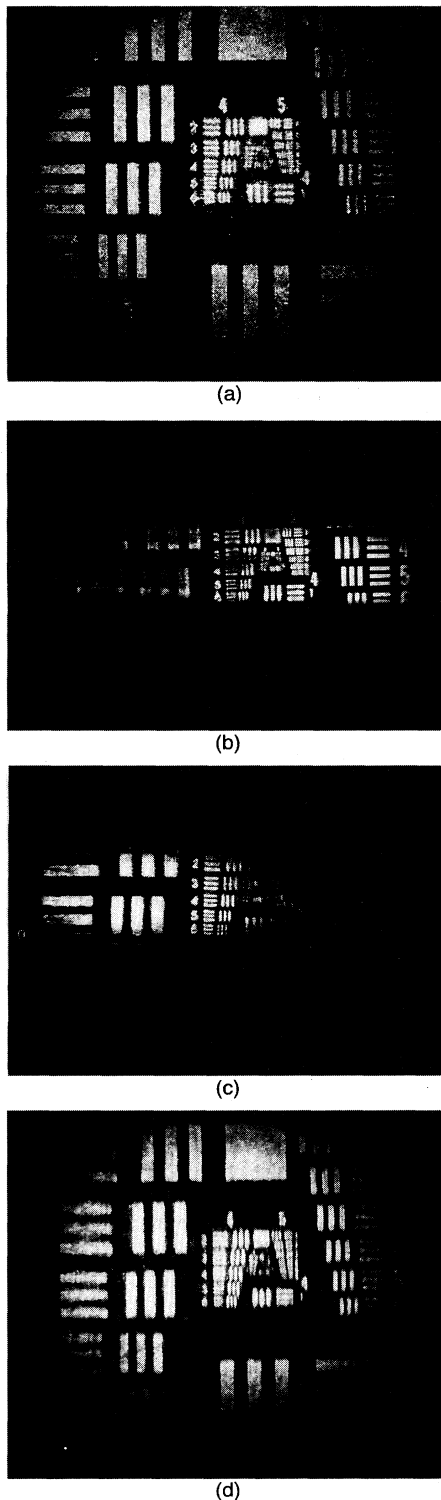


FIG. 6. The input image of (a) a resolution chart and (b)–(d) the reconstructed images produced by a BaTiO₃ TIR mirror. (b) The crystal is in the image plane, the intensity distribution shifts to the right, in the direction of fanning. (c) The same as (b) but with the *c* axis flipped 180°; the shift is in the opposite direction. (d) The crystal is placed 40 mm before the image plane of the chart.

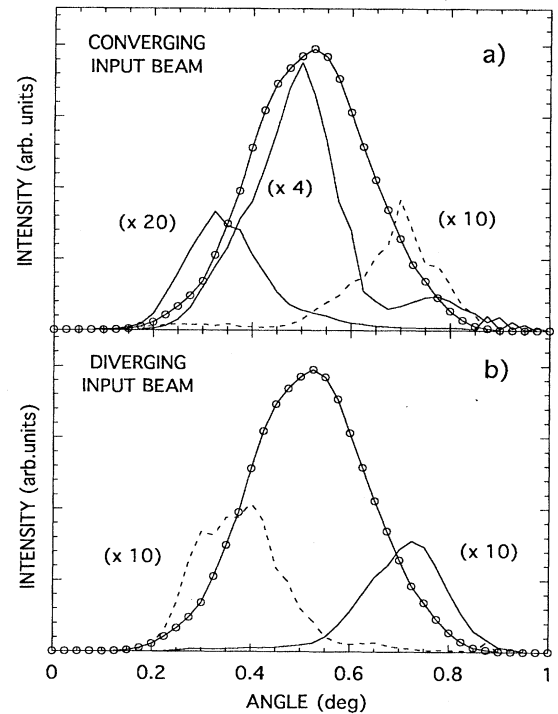


FIG. 7. Angular shift of the phase-conjugate beam for (a) a converging and (b) a diverging input beam. The dotted curves show the angular spectrum of the input beam, the solid curves are the angular spectra of the conjugate beam for the incident beam fanning to the right in the crystal, and the dashed curves are the same for the beam fanning to the left.

higher than that in the imaging case. The reason is that the reproduction of the input image in itself is not a guarantee of good phase-conjugation fidelity. For example, wedge-type distortions (different direction of propagation of the phase-conjugate beam) may not be visualized with this technique.

To study possible phase distortions that may lead to a conjugate beam not exactly counterpropagating with the input beam, we have conducted the following experiment. An input Gaussian beam was focused by a $f = 260$ mm lens. The photorefractive BaTiO₃ crystal was placed at a distance d from the lens, in either the converging ($d = 200$ mm) or diverging region of the beam ($d = 320$ mm). The far-field intensity distribution of the phase-conjugate beam was compared with the one of the input beam being exactly retroreflected by a mirror placed in the focal plane. The convergence or divergence angle for the input beam for these parameters was $\approx 0.3^\circ$. Figure 7 shows results of this experiment for the converging (a) and diverging (b) cases. The dotted curves give the angular spectrum of the input Gaussian beam. The solid and dashed curves are the angular spectra of the conjugate beam, corresponding to two opposite directions of the *c* axis, that is, to the beam fanning either to the right or to the left in the laboratory frame, respectively. The angles lying to the left of the peak of the input Gaussian correspond to rays leaving the crystal on the left side of the nominal direction of the exactly counterpropagating beam, and vice versa. The maximum in the angular spectrum of the phase-conjugate beam is clearly shifted with respect to that

of the input beam. Reversing the direction of fanning flips the shift, confirming the noncollinear nature of the effect. A comparison of the two solid curves in Fig. 7 (a) shows that the angular spectrum of the conjugate beam becomes more like that of the incident beam when the reflectivity is increased from $\approx 2\%$ ($\times 20$ curve) to $\approx 25\%$ ($\times 4$ curve). This is in agreement with theoretical calculations, confirming that the conjugation fidelity in the geometry of the TIR mirror increases with an increase in the reflectivity. Low reflectivities give rise to large angular shifts, which is also reflected in a considerable drop in fidelity [see Figs. 1(a) and 1(b)]. Finally, Figs. 7(a) and 7(b) show that for the same direction of bending the direction of the shift is directly dependent on whether the beam is converging or diverging. A beam fanning to the right produces a conjugate beam whose angular spectrum is shifted to the left of the nominal direction of propagation of an ideally backscattered beam for the converging case, and to the right for the diverging case. These directions are in perfect agreement with the numerical results discussed in Sec. III and shown in Figs. 2(b) and 3(a).

V. CONCLUSIONS

We have analyzed the geometry of the total-internal-reflection phase-conjugate mirror in the framework of a two-dimensional model. This model is based on the solution of the paraxial equations for the electromagnetic radiation and the equation for the material response of the medium. It consistently takes into account both diffraction and two-dimensional effects due to the finite transverse size and the noncollinearity of the interacting beams. For certain orientations of the input beam and the crystal faces, the beam evolution inside the medium as described by our model results in a natural way in the formation of the spatial structure of fields corresponding to the operation of the TIR mirror. The calculated spatial structure of light and the refractive index inside the nonlinear medium indicates that the TIR mirror is a distributed phase conjugator. Phase conjugation takes place not only in the main body of the beam but also inside the loops formed by the fanning of this beam.

The TIR mirror requires a finite level of seeds for its operation; both the nonlinear reflectivity R and the conjugation fidelity H have been found to directly depend on the level of these seeds. Larger seeds give rise to higher values of R and H . The fidelity is somewhat less dependent on the

level of seeds than the nonlinear reflectivity. The fidelity also reaches its steady-state value earlier than the nonlinear reflectivity. The same qualitative behavior is exhibited by other self-pumped four-beam mixing geometries (see, e.g., [7]).

The far- and near-field distributions of the scattered radiation have been calculated and analyzed in detail. It has been found that phase conjugation in the geometry of the TIR mirror is accompanied by reproduction of small-scale structure and by large-scale distortions of the beam envelope both in space and in Fourier domains, or, in other words, intensity and phase distortions. This statement does not mean that the TIR mirror is not a phase conjugator; it simply reflects the fact that its performance, as that of any real device, is not ideal. We have analyzed both the nature of the distortions and their dependence on the parameters of the problem. These questions have not been previously addressed either theoretically or experimentally, partially because of the lack of theoretical predictions. In particular, we have found that the magnitude of the distortions is most pronounced for small values of the nonlinearity and/or the level of seeds and decreases when either of these parameters is increased. Higher values of the nonlinear reflectivity and conjugation fidelity correspond to lower distortions. The distortions of the intensity profile of the conjugate beam correspond to its shift in the direction of convective flow of energy for the scattered radiation (the direction of fanning). The phase distortions correspond to a shift in the spectrum of the conjugate beam with respect to that of the incident one. In general, the conjugate beam does not propagate exactly back with respect to the incident one. The output direction of propagation may lie on either side of that of the incident beam and is determined mostly by the focusing conditions.

Despite good agreement between the predictions of theory and experiment, the theoretical model cannot be considered exhaustive. First, it accounts for only one transverse dimension. Second, the structure of the electrooptic tensor in many photorefractive media is more complex than that assumed by the material equation (3). Thus the model does not contain reflection gratings, that is, nonlinear changes in the refractive index corresponding to the direct backscattering $\vec{k} \rightarrow -\vec{k}$, where \vec{k} is the wave vector of the incident beam. Such gratings have been shown to exist in photorefractive materials [17,18], and can be important in some cases. The existence of the reflection gratings in the geometry of the TIR mirror may decrease the effects of noncollinearity, resulting in shifts in both the space and the Fourier domains as compared to those predicted by our model.

-
- [1] J. Feinberg, *Opt. Lett.* **7**, 486 (1982).
 - [2] V. V. Voronov, I. R. Dorosh, Yu. S. Kuz'minov, and N. V. Tkachenko, *Kvant. Elektron. (Moscow)* **7**, 1234 (1980) [*Sov. J. Quantum Electron.* **10**, 1346 (1980)].
 - [3] K. R. MacDonald and J. Feinberg, *J. Opt. Soc. Am.* **73**, 548 (1983).
 - [4] A. A. Zozulya, *IEEE J. Quantum Electron.* **29**, 538 (1993)
 - [5] M. Cronin-Golomb, *Opt. Commun.* **89**, 276 (1992).
 - [6] A. A. Zozulya, M. Saffman, and D. Z. Anderson, *Phys. Rev. Lett.* **73**, 818 (1994).
 - [7] A. A. Zozulya, M. Saffman, and D. Z. Anderson, *J. Opt. Soc. Am. B* **12**, 255 (1995).
 - [8] A. A. Zozulya and D. Z. Anderson, *Phys. Rev. A* **51**, 1520 (1995).
 - [9] N. V. Kukhtarev, V. B. Markov, S. G. Odulov, M. S. Soskin, and V. L. Vinetskii, *Ferroelectrics* **22**, 949 (1979).
 - [10] T. R. Moore and D. L. Walther, *J. Opt. Soc. Am. B* **5**, 1806 (1988).
 - [11] M. Segev, Y. Ofir, and B. Fischer, *Opt. Commun.* **77**, 265 (1990).

- [12] J. J. Liu and P. Banerjee, *J. Opt. Soc. Am. B* **11**, 1688 (1994).
- [13] A. A. Zozulya and D. Z. Anderson, *Phys. Rev. A* **52**, 878 (1995).
- [14] E. Parshall, M. Cronin-Golomb, and R. Barakat, *Opt. Lett.* **20**, 432 (1995).
- [15] V. T. Tikhonchuk and A. A. Zozulya, *Prog. Quantum Electron.* **15**, 231 (1991).
- [16] S. Weiss, S. Sternklar, and B. Fischer, *Opt. Lett.* **12**, 114 (1987).
- [17] M. Z. Zha and P. Günter, *Opt. Lett.* **10**, 184 (1985).
- [18] S. A. Korol'kov, A. V. Mamaev, and V. V. Shkunov, *Int. J. Nonlin. Opt. Phys.* **2**, 157 (1993).

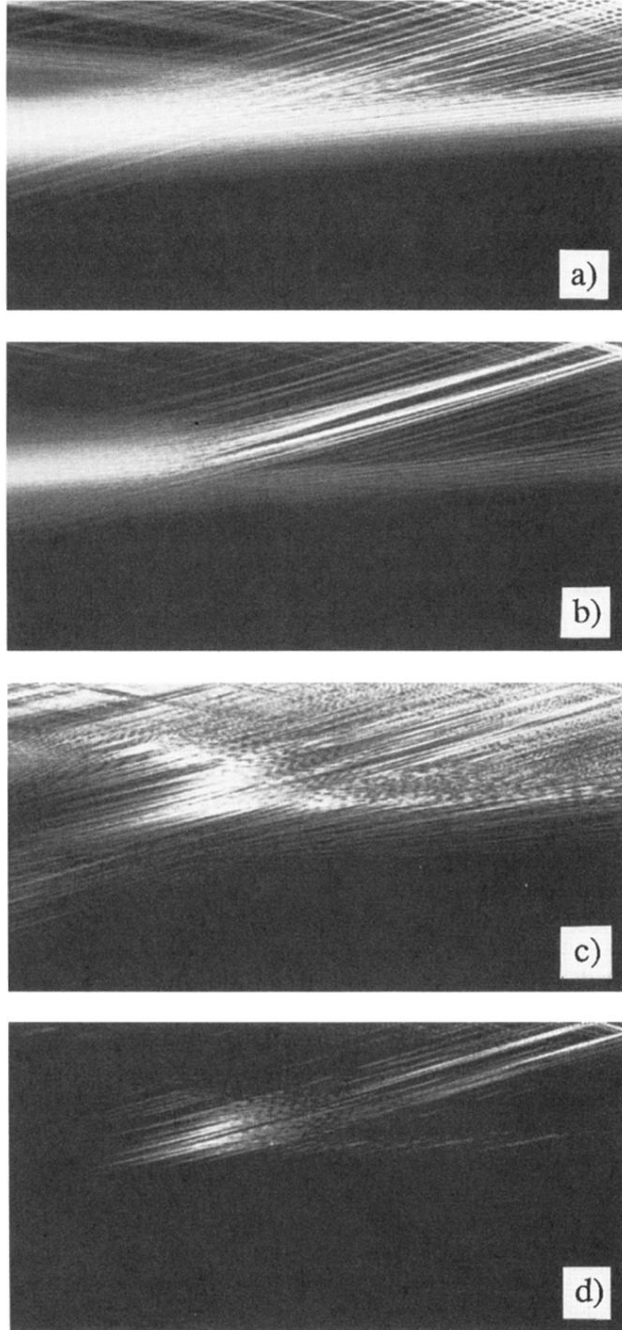
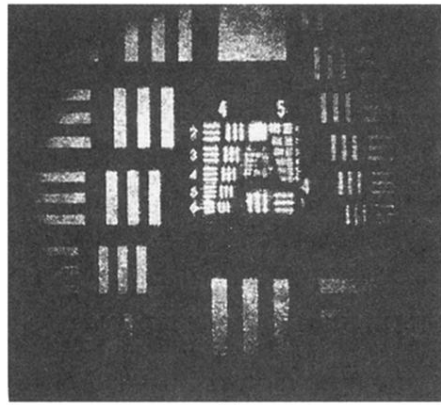
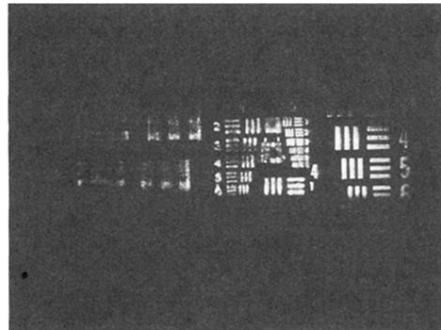


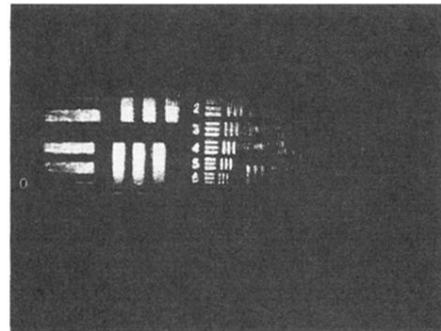
FIG. 5. Spatial distribution of the total light intensity $\tilde{I}_{em} = |A_f|^2 + |A_b|^2$ inside the crystal for (a) $t=5$ and (b) $t=60$; (c) spatial distribution of the modulus of the refractive index ν for $t=60$; and (d) the product $P = \tilde{I}_{em} \nu^2$ for $t=60$. The size of the computation region for all figures is $l_x = 1.5$ mm and $l_y = 0.52$ mm along the x and y coordinate axes, respectively.



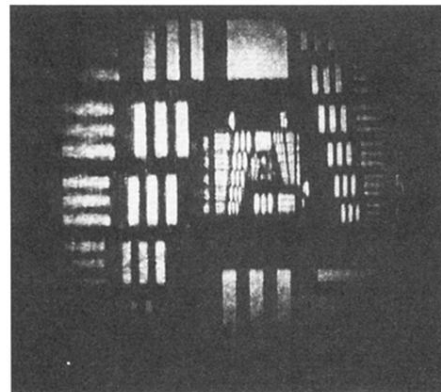
(a)



(b)



(c)



(d)

FIG. 6. The input image of (a) a resolution chart and (b)–(d) the reconstructed images produced by a BaTiO_3 TIR mirror. (b) The crystal is in the image plane, the intensity distribution shifts to the right, in the direction of fanning. (c) The same as (b) but with the c axis flipped 180° ; the shift is in the opposite direction. (d) The crystal is placed 40 mm before the image plane of the chart.